HHS Public Access

Author manuscript

Nano Lett. Author manuscript; available in PMC 2019 January 10.

Published in final edited form as:

Nano Lett. 2018 January 10; 18(1): 182–189. doi:10.1021/acs.nanolett.7b03829.

Janus Iron Oxides @ Semiconducting Polymer Nanoparticle Tracer for Cell Tracking by Magnetic Particle Imaging

Guosheng Song[1], **Min Chen**[1], **Yanrong Zhang**[2], **Liyang Cui**[1], **Haibo Qu**[2], **Xianchuang Zheng**[1], **Max Wintermark**[2], **Zhuang Liu**[3], and **Jianghong Rao**[1,*]

[1]Molecular Imaging Program at Stanford, Department of Radiology, Stanford University School of Medicine, 1201 Welch Road, Stanford, California, 94305-5484, USA

[2]Department of Radiology, Neuroimaging and Neurointervention Division Stanford University Hospital 300 Pasteur Drive, Stanford, CA 94305, USA

[3]Institute of Functional Nano and Soft Materials (FUNSOM), Jiangsu Key Laboratory for Carbon-based Functional Materials and Devices, Soochow University, Suzhou, Jiangsu 215123, China

Abstract

Iron oxides nanoparticles tailored for magnetic particle imaging (MPI) have been synthesized, and their MPI signal intensity is 3 times of commercial MPI contrast (Ferucarbotran, also called Vivotrax) and 7 times of MRI contrast (Feraheme) at the same Fe concentration. MPI tailored iron oxide nanoparticles were encapsulated with semiconducting polymers to produce Janus nanoparticles that possessed optical and magnetic properties for MPI and fluorescence imaging. Janus particles were applied to cancer cell labeling and *in vivo* tracking, and as few as 250 cells were imaged by MPI after implantation, corresponding to an amount of 7.8 ng of Fe. Comparison with MRI and fluorescence imaging further demonstrated the advantages of our Janus particles for MPI—super sensitivity, unlimited tissue penetration and linear quantitativity.

TOC image

Janus Fe_3O_4 @ semiconducting polymer nanoparticles have been developed for cell labeling and *in vivo* tracking by MPI and fluorescence imaging with high MPI sensitivity.

*Correspondence and requests for materials should be addressed to J. Rao. (jrao@stanford.edu).

Supporting Information

Supplementary Information accompanies this paper: Experimental procedures and supporting Figures S1–7.

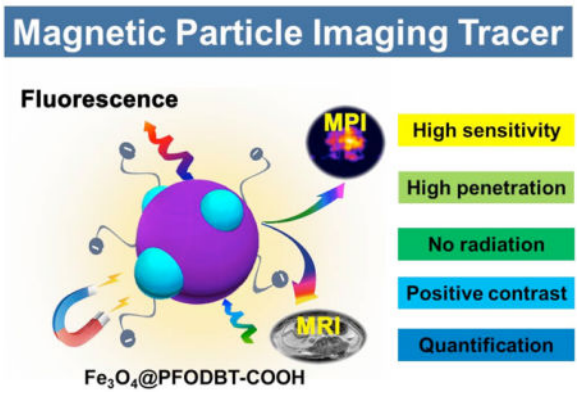

Keywords

magnetic particle imaging; iron oxides; semiconducting polymer; cell tracking

Introduction

Cell-based therapies, such as cancer immunotherapy or stem-cell therapy, have received considerable attention as novel therapeutics in oncological research.[1] These therapeutic strategies require noninvasive imaging technologies to track the location of therapeutic cells after being introduced into the body in real time, and to report the biological fate, activation and differentiation of therapeutic cells, ideally at the single-cell sensitivity and resolution at any tissue depth.[2–4] Current cell-tracking techniques use magnetic resonance imaging (MRI), radionuclide imaging (e.g. single-photon emission computed tomography (SPECT), positron emission tomography (PET)), or optical imaging (fluorescence, bioluminescence, photoacoustic).[3] While optical imaging typically offers remarkably high sensitivity, light photon is strongly absorbed and scattered as it penetrates biological tissues, which makes it difficult to image in deep tissues non-invasively;[5,6] even in the wavelength range between 1000–1700 nm, the tissue penetration depth is just around several millimeters.[7,8] MRI offers excellent depth penetration and high spatial resolution, however, the T1 contrast agents show poor sensitivity for molecular imaging, and T2 or T2* contrast agents such as iron oxide nanoparticles produce a negatively enhanced contrast that is difficult to distinguish from tissues with naturally low MRI signal (e.g., bones, lungs).[2,9–12] Radionuclide imaging requires the use of radioactivity and has low spatial resolution; for long-term tracking, therapeutic cells have to be genetically labeled with a reporter gene and imaged with repetitive injections of radionuclide tracers.[13–15]

Magnetic particle imaging (MPI) is a new imaging modality that was initially proposed by Gleich and Weizenecker to use time-varying magnetic fields to directly detect iron oxide nanoparticles, rather than indirectly via MRI signal dropouts.[16,17] Compared with existing modalities, MPI promises high depth penetration, linear quantitativity, positive contrast, no radiation, and nearly no background from tissues.[18–20] Moreover, iron oxide nanoparticles have already been tested to be safe for MR imaging in clinical use.[21–23] Recently, MPI have been reported for tracking of iron-oxide nanoparticle labeled stem cells or macrophages, and

for imaging of brain injury, vascular, lung perfusion and xenografted tumor in animals.[19,21,22,24–28] Notably, MP imaging abilities are highly dependent on magnetic nanoparticles as tracer.[16,17] While existing superparamagnetic iron oxide nanoparticles have been extensively developed for MR imaging, unfortunately, they are suboptimal for MPI as reported because their magnetic core size is small (typically <10 nm in diameter).[19,22] Gleich and Weizenecker estimated a detection limit to be about 100 μM of Fe with current commercial MR contrast agent Resovist, but their calculation suggested MPI could reach a possible detection limit of 20 nM of Fe with improvements in iron oxide nanoparticles and recording electronics.[16] Therefore, the realization of the full potential of MPI to the sensitivity of PET heavily depends on the availability of magnetic tracers tailored to MPI's unique physics. However, just a few publications report the effort on improving iron oxide nanoparticles for MPI application, primarily focusing on tuning the magnetic core size.[26,27,29–31]

Herein, we have systemically investigated the reaction conditions required for synthesizing iron oxide nanoparticles with high MPI signals. We further encapsulated synthesized iron oxide nanoparticles in fluorescent semiconducting polymers to afford Janus Fe_3O_4@semiconducting polymer nanoparticles. Each Janus particle was found to contain two or more Fe_3O_4 nanoparticles, but they displayed the same MPI signal intensity as non-encapsulated Fe_3O_4 nanoparticles when compared at the same concentration of Fe. As few as 250 HeLa labeled by Janus particles (with the average uptake of Fe at 31 pg/cell) can be imaged by the commercial MPI scanner after implantation in mice, corresponding to an amount of 7.8 ng of Fe. To the best of our knowledge, this work represents the first example of Janus fluorescent MPI-tailored tracers that enable MPI, MRI, and fluorescence imaging for cell tracking *in vivo*.

Results and discussion

We first probed the reaction parameters to synthesize iron oxide nanoparticles with high MPI signals. Our nanoparticle synthesis used thermal decomposition of iron-oleate complex in the presence of oleic acid.[32] We first fixed the reaction temperature at 310 °C, varied the reaction times (e.g. 0.5, 5, 10, 21, 31, 48 h) in our synthesis. As TEM images (Figure 1a) show, the as-synthesized iron oxide nanoparticles displayed uniform size. Their average diameters slightly increased from 14.1 nm to 16.2 nm, as the reaction time extended from 0.5 h to 48 h. Powder X-ray diffraction (XRD) patterns (Figure 1b) revealed that the iron oxide nanoparticles synthesized at 0.5 h was cubic FeO (JCPDS card file no: 06-0615). When the reaction time increased to 21 h, the as-synthesized iron oxide nanoparticles were gradually converted from cubic FeO to cubic Fe_3O_4 (JCPDS card file no: 65-3107). When the reaction time increased to 31 h, the crystallinity of the cubic Fe_3O_4 also increased, but showed the decrease at 48 h.

The as-prepared iron oxides nanoparticles were coated with a layer of hydrophobic oleic acid at the surface. Thus, the copolymer poly(styrene-co-maleic anhydride) (PSMA) was introduced to modify the iron oxide particles through the hydrophobic interaction between the oleate layer and the styrene units in PSMA at the surface. Subsequent hydrolysis of maleic anhydride in PSMA presented the surface with carboxyl groups. As-prepared Fe_3O_4-

COOH nanoparticles were well dispersed in PBS with an average size of 27 nm in diameter determined by DLS (Figure 2c), and zeta potential of −26.3 mV. The MPI contrast abilities of these PSMA modified water-soluble iron oxide nanoparticles were measured by a MPI scanner (Figure S1). Figure 1c plots the MPI signals of iron oxides nanoparticles at the same amount of Fe (8 μg) versus the reaction times, indicating the peak of the MPI signal at 31 h. Interestingly, although the iron oxide nanoparticles prepared at 21 h have similar sizes to those prepared at 10 h, their MPI signals exhibited great difference, suggesting that the crystallinity of the cubic Fe_3O_4 is important to the MPI contrast ability of iron oxide nanoparticles.

Next, we examined the effect of the reaction temperature and slightly decreased it to 280 °C from 310 °C. The iron oxide nanoparticles synthesized at 280 °C/ 21 h were monodisperse but had a smaller size—11.4 nm in diameter (Figure 1d). They were also cubic Fe_3O_4 but with lower crystallinity (Figure 1e), and surprisingly, after PSMA modification their MPI signal was just about 1/10th of particles prepared at 310 °C/ 21 h (Figure 1f). When the iron oxide nanoparticles synthesized at 310 °C/21 h were annealed at 600 °C for 2 h in the air atmosphere, the nanoparticles were fused together into large particles without regular morphologies, as shown by TEM (Figure 1d). XRD indicated that cubic Fe_3O_4 was completely oxidized to hexagonal Fe_2O_3 (JCPDS card file no: 33-0664) (Figure 1e). Consequentially, no MPI signals were detectable in annealed nanoparticles (Figure 1f). Therefore, our results have shown that the MPI signal is greatly dependent on the crystalline structure of the iron oxide nanoparticles and the cubic Fe_3O_4 structure is required for high MPI signals.

The MPI signal of Fe_3O_4-COOH nanoparticles were compared with commercial MPI contrast agent ferucarbotran and commercial MRI contrast agent Feraheme. Ferucarbotran is available as Vivotrax from Magnetic Insight Inc. (USA) and has the same performance as Resovist from Bayer Schering (not available any more). The MPI signal generated by the Fe_3O_4-COOH nanoparticles prepared at 310 °C/31 h is 3 times of that of Vivotrax (Figure 1g) and 7 times that of Feraheme (Figure S2) at the same concentration of Fe. Figures 1h and S3 plot the linear dependence of the MPI signals on the concentration of Fe for Fe_3O_4-COOH particles and Vivotrax, but the slope for Fe_3O_4-COOH particle (80.6 μg^{-1}) is much higher than that of Vivotrax (24.2 μg^{-1}).

Semiconducting polymer nanoparticles have been shown to possess unique optical properties for fluorescence and photoacoustic imaging.[33,34] From both the views of nanomaterials and cell tracking, it would be interesting to fuse iron oxide nanoparticles with semiconducting polymer nanoparticles and produce Janus nanoparticles that can be imaged fluorescently and by MPI. To prepare such Janus nanoparticles, we used a nanoprecipitation method (Figure 2a):[35–38] a THF solution containing 0.25 mg of semiconducting polymer (PFODBT, Poly[2,7-(9,9-dioctylfluorene)-alt-4,7-bis (thiophen-2-yl)benzo-2,1,3-thiadiazole]), 1 mg of oleic acid coated Fe_3O_4 nanoparticles, and 2 mg of PSMA was rapidly injected into H_2O under sonication. Similar to the Fe_3O_4-COOH nanoparticles, the as-prepared Fe_3O_4@PFODBT Janus particles also possessed carboxyl groups at the surface after hydrolysis of the maleic anhydride on the PSMA. After the removal of THF by rotary evaporation and filtration, the nanoparticles were dissolved in water. TEM image indicated

these Janus particles at a size of about 42.3 nm in diameter, with iron oxide nanoparticles embedded in the polymer matrix (Figure 2b). As-prepared Fe_3O_4@PFODBT-COOH nanoparticles were well dispersed in PBS with an average size of 51 nm determined by DLS (Figure 2c), and zeta potential of −32.4 mV. The Janus particles inherited the characteristic absorption peaks of both PFODBT and Fe_3O_4-COOH nanoparticles (Figure 2d), and exhibited fluorescence emission at 680 nm when exited at 540 nm (Figure 2e). MPI contrast ability of Fe_3O_4@PFODBT-COOH Janus nanoparticles was compared to Fe_3O_4-COOH nanoparticles. From the two dimensional projection of MPI and line MPI spectrum (Figure 2f), the Fe_3O_4@PFODBT-COOH Janus nanoparticles displayed the same contrast ability as Fe_3O_4-COOH nanoparticles. Moreover, the MPI signals of Fe_3O_4@PFODBT-COOH are also linear over a broad range concentration of Fe (R^2=0.999, Figure 2g). To our delight, the PFODBT polymer encapsulation did not produce any effect on the MPI signal intensity of Fe_3O_4-COOH. The spatial resolution of Fe_3O_4@PFODBT-COOH for MPI was also evaluated: two microbore tubes filled of Fe_3O_4@PFODBT-COOH were placed in the MPI scanner for two-dimensional projection imaging (Figure S4). At the edge-to-edge distance of 2.5 mm, their MP images are well separated and the significant minimum between them is at the half height of the maximum intensity (Figure S4).

We next explored the use of Fe_3O_4@PFODBT-COOH Janus particles for cell labeling and imaging. Human cervical cancer HeLa cells were chosen as a model and incubated with Fe_3O_4@PFODBT-COOH (at 60 μg of Fe/mL) in serum-free culture medium for 4 h before washing with PBS for three times to remove unbounded particles.[39,40] The confocal imaging (Figure 3a) showed discrete red fluorescent dots located around the nucleus. The observed red fluorescence emission was from the semiconducting polymers on the Janus nanoparticles, indicating that Fe_3O_4@PFODBT-COOH nanoparticles were taken up into HeLa cells. The cellular uptake of particles was further quantified by ICP-MS measurement to measure the concentration of Fe, revealing a positive correlation with the incubation concentration (Figure 3b). Specifically, at the incubation concentration of 60 μg of Fe/mL, the average uptake was 31 pg Fe /cell. After labeling, these particles did not produce notably influence on the cell viabilities even after 48 h further incubation (Figure 3c), assayed by MTS, suggesting that the as-prepared Fe_3O_4@PFODBT-COOH was biocompatible with low toxicity, when used as a tracer for cell labeling.

After cells were labeled by the Janus particles (31 pg Fe/cell), a series of diluted samples with the number of cells from 2,500 to 640,000 in a 200 μL PCR tube were scanned by two-dimensional MPI, fluorescence and MR imaging. As shown in Figure 3d, the MPI signals are linearly correlated to the cell number (R^2=0.998). 2,500 labeled HeLa cells gave a signal-to-background ratio (defined as (signal-background)/background) of 1.76, estimated from the linear scanning MPI spectrum (Figure 3e). The number of cells that can be imaged can be further reduced by increasing the scan project number and background subtraction.[41,42] For example, with the 2D Average/ Time Course MPI scanning and using 25 of projection number, 500 labeled cells (31 pg Fe/cell) can be imaged with the signal-to-background ratio of 3.20 (Figure 2f) after subtraction of the background signal from a blank sample (Figure S5a), and 250 labeled cells can be clearly visualized as well with the signal-to-background ratio of 2.03 (Figure 2g & S5b).

In comparison, while fluorescence imaging of labeled cells under the same conditions (excitation at 540 nm, emission at 680 nm) showed good a linear correlation between the fluorescence signals and the cell number (Figure 3h), the signal-to-background ratio of 2500 labeled cells in fluorescence imaging is only 0.11 (Figure S6). For T_2-weighted MRI, the signals of T_2-weighted MRI produced by labeled cells was not linearly dependent on the cell number (Figure 3i).

Next, Fe_3O_4@PFODBT-COOH labeled HeLa cells were implanted into a living mouse for whole-body fluorescence, MPI and MRI to directly compare the imaging contrast and depth attenuation of these three imaging modalities *in vivo*. As shown in Figure 4a, 30,000 labelled cells subcutaneously injected onto the abdomen area of the mouse produced strong signal in fluorescence imaging at the front view, but no fluorescence signal could be detected when the mouse was imaged from the back view, due to the limited penetration of fluorescence light. The autofluorescence from the animal, especially the fur significantly compromised the detection sensitivity. After removing the fur around the abdomen area, about 2,500 labeled cells could be seen by fluorescence imaging (Figure 4b). In comparison, the same 30,000 labelled cells implanted in the same mouse were visualized by 2-D projection MPI with high contrast at both the front and back views: the signal to noise ratio is 16.1 (Figure 4c). With 2,500 labeled cells subcutaneously implanted onto the back, 2-D projection MPI showed the signal-to-noise ratio of 1.3 (Figure 4d). 3-D MPI can be fused with CT image (Figure 4e and S7) to show the location of labeled cancer cells in the mouse body. When the number of labeled cells decreased further, the MPI signal was low, but if we used the background subtraction method, 250 cells were able to be visualized after local injection onto back (Figure 4f). On the other hand, MR imaging of labeled cancer cells is more challenging since the iron oxide nanoparticles produces a dropout signal similar to dark signal at air-tissue interfaces. For example, negative contrast of 2500 labeled cells was hardly distinguishable in T_2-weight MRI (Figure 4g).

To evaluate Fe_3O_4@PFODBT-COOH for longitudinal cell tracking, HeLa cells xenografts were established by subcutaneously implantation of Hela cells (3.5×10^5) pre-labelled with Fe_3O_4@PFODBT-COOH into mice (n = 3). Fluorescence and MPI images were acquired every other day from day 10 post implantation. Strong fluorescence could be detectable from tumor area from day 10 to day 20 post implantation (Figure 4h). Meanwhile, serial MPI images showed high signal contrast in tumor area with no detectable signal from surrounding anatomy (Figure 4j). Moreover, the fluorescence and MPI signals only decreased by about 20 % after 10 days of growth (Figure 4i & k). 3-D MPI/CT imaging (Figure 4l) correlated the MPI signal with the anatomic location of the tumor mass originated from the labeled cancer cells. On day 20 post implantation, the tumors were dissected, frozen, sliced, fixed and stained with DAPI for fluorescence imaging, which showed strong red fluorescence in tumor slice from the fluorescent semiconducting polymers on the Janus particles (Figure 4m). These results have demonstrated that the Janus nanoparticle Fe_3O_4@PFODBT-COOH has the potential for in vivo long-term cell tracking by MPI and fluorescence imaging.

Since its conception, MPI has been shown great potential as a new imaging modality for molecular imaging. As our results present, MPI can image the magnetic tracer at any tissue

depth with a positive contrast, and there is an excellent linearity between the tracer amount and the signal intensity. The magnetic tracers, mainly iron oxide nanoparticles, are the key to the sensitivity of MPI. Unfortunately, existing iron oxide nanoparticles are not tailored to the MPI physics. In this work, we probed the reaction parameters to tailor the synthesis of iron oxide nanoparticles for MPI. Our results have shown that MPI signal is also greatly dependent on the particle' crystalline structures, in addition to the particles' sizes. Interestingly, the diameter of the iron oxide core of our particles is about 16 nm, while previous works suggest the optimal size of iron oxide core of MPI SPIO nanoparticles is around 24–26 nm in diameter. Thus, to optimize the particles for MPI, both particle' sizes and crystallinities should be carefully controlled. The MPI signal of iron oxide nanoparticles synthesized under our optimized condition is 3 times of that of Vivotrax, and 7 times that of Feraheme at the same concentration of Fe. Thus, the sensitvity of our Janus iron oxide nanoparticles is comparable to that of Krishnan's tailored nanoparticles.[43,44] While the endogenous background noise of MPI is extremely low, we found that this low level background may be subtracted to improve the imaging sensitivity when an extremely low amount of tracer was used—a few nanograms of Fe. With further advance in the MPI hardware, for example, a new gradiometric receive-coil recently reported by Buzug et al,[45] the MPI sensitivity of our particles may be further improved.

The coating chemistry developed here allows our MPI tailored iron oxide nanoparticles to be encapsulated with semiconducting polymers to produce Janus nanoparticles, in which the optical property of the polymer and magnetic property of the iron oxide nanoparticles are integrated for MPI and fluorescence imaging. The fluorescence emissions of Janus nanoparticles can be tuned up with different semiconducting polymers, and maybe even afford photoacoustic contrast ability since semiconducting nanoparticles have been shown as excellent photoacoustic imaging agents.[35,46] The dual or more modalities imaging facilitates cell imaging at multiple settings from *in vitro* to *in vivo*. We evaluated the performance of the Janus particles for cell labeling and *in vivo* tracking, and as low as 250 cells could be imaged by MPI after implantation in the mouse body without depth limitation. With further optimization of the loading efficiency and the improvement of the particle imaging performance, tens of or even single labeled cells may be imaged by MPI.

Conclusion

In conclusion, our investigation into synthesizing MPI tailored iron oxides (Fe_3O_4), has shown that temperature and reaction time affects the quality of cubic Fe_3O_4 crystal in the nanoparticles, and thus the MPI imaging intensity. Our synthetic condition provided iron oxide nanoparticles that displayed 3 times MPI signal of commercial MPI tracer (Vivotrax) and 7 times that of MRI contrast agent (Feraheme) at the same concentration of Fe. Janus nanoparticles made by encapsulating iron oxide nanoparticles in semiconducting polymers allowed efficient cell labeling and sensitive MPI tracking after implantation into mice. While Janus nanoparticles are applied to cell tracking here, they may enable other MPI applications, such as multimodality cancer imaging after particle functionalization with tumor-targeting ligands.

Supplementary Material

Refer to Web version on PubMed Central for supplementary material.

Acknowledgments

The authors acknowledge the use of Stanford Center for Innovation in In-Vivo Imaging (SCI^3) Core Facility. This work was supported by the National Institutes of Health (NIH) grants R01DK099800 and the Stanford University National Cancer Institute (NCI) CCNE-T grant (U54CA151459).

References

1. Weber J, Atkins M, Hwu P, Radvanyi L, Sznol M, Yee C. Clin Cancer Res. 2011; 17:1664. [PubMed: 21325070]
2. Ahrens ET, Bulte JW. Nat Rev Immunol. 2013; 13:755. [PubMed: 24013185]
3. Kircher MF, Gambhir SS, Grimm J. Nat Rev Clin Oncol. 2011; 8:677. [PubMed: 21946842]
4. Weissleder R, Nahrendorf M, Pittet MJ. Nat Mater. 2014; 13:125. [PubMed: 24452356]
5. Sutton EJ, Henning TD, Pichler BJ, Bremer C, Daldrup-Link HE. Eur Radiol. 2008; 18:2021. [PubMed: 18506449]
6. Song G, Hao J, Liang C, Liu T, Gao M, Cheng L, Hu J, Liu Z. Angew Chem Int Ed. 2016; 55:2122.
7. Hong G, Antaris AL, Dai H. Nat Biomed Eng. 2017; doi: 10.1038/s41551
8. Hong G, Lee JC, Robinson JT, Raaz U, Xie L, Huang NF, Cooke JP, Dai H. Nat Med. 2012; 18:1841. [PubMed: 23160236]
9. Bulte JW. Am J Roentgenol. 2009; 193:314. [PubMed: 19620426]
10. Song G, Liang C, Gong H, Li M, Zheng X, Cheng L, Yang K, Jiang X, Liu Z. Adv Mater. 2015; 27:6110. [PubMed: 26331476]
11. Zeng J, Jing L, Hou Y, Jiao M, Qiao R, Jia Q, Liu C, Fang F, Lei H, Gao M. Adv Mater. 2014; 26:2694. [PubMed: 24615901]
12. Dahnke H, Schaeffter T. Magnet Reson Med. 2005; 53:1202.
13. Hong H, Yang Y, Zhang Y, Cai W. Curr Top Med Chem. 2010; 10:1237. [PubMed: 20388105]
14. Srinivas M, Aarntzen E, Bulte J, Oyen W, Heerschap A, De Vries I, Figdor C. Adv Drug Deliver Rev. 2010; 62:1080.
15. Gu E, Chen W-Y, Gu J, Burridge P, Wu JC. Theranostics. 2012; 2:335. [PubMed: 22509197]
16. Gleich B, Weizenecker J. Nature. 2005; 435:1214. [PubMed: 15988521]
17. Goodwill PW, Saritas EU, Croft LR, Kim TN, Krishnan KM, Schaffer DV, Conolly SM. Adv Mater. 2012; 24:3870. [PubMed: 22988557]
18. Pablico-Lansigan MH, Situ SF, Samia AC. Nanoscale. 2013; 5:4040. [PubMed: 23538400]
19. Zheng B, Vazin T, Goodwill PW, Conway A, Verma A, Saritas EU, Schaffer D, Conolly SM. Sci Rep. 2015; 5:14055. [PubMed: 26358296]
20. Goodwill PW, Conolly SM. IEEE T Med Imaging. 2010; 29:1851.
21. Yu EY, Bishop M, Zheng B, Ferguson RM, Khandhar AP, Kemp SJ, Krishnan KM, Goodwill PW, Conolly SM. Nano Lett. 2017; 17:1648. [PubMed: 28206771]
22. Zheng B, von See MP, Yu E, Gunel B, Lu K, Vazin T, Schaffer DV, Goodwill PW, Conolly SM. Theranostics. 2016; 6:291. [PubMed: 26909106]
23. Wu L, Mendoza-Garcia A, Li Q, Sun S. Chem Rev. 2016; 116:10473. [PubMed: 27355413]
24. Zhou XY, Jeffris KE, Elaine YY, Zheng B, Goodwill PW, Nahid P, Conolly SM. Phys Med Biol. 2017; 62:3510. [PubMed: 28218614]
25. Orendorff R, Peck AJ, Zheng B, Shirazi SN, Ferguson RM, Khandhar AP, Kemp SJ, Goodwill P, Krishnan KM, Brooks GA. Phys Med Biol. 2017; 62:3501. [PubMed: 28378708]
26. Kraupner A, Eberbeck D, Heinke D, Uebe R, Schüler D, Briel A. Nanoscale. 2017; 9:5788. [PubMed: 28447690]

27. Starmans LW, Burdinski D, Haex NP, Moonen RP, Strijkers GJ, Nicolay K, Grüll H. PLoS One. 2013; 8:e57335. [PubMed: 23437371]
28. Knopp T, Gdaniec N, Möddel M. Phys Med Biol. 2017; 62:R124. [PubMed: 28398219]
29. Tomitaka A, Arami H, Gandhi S, Krishnan KM. Nanoscale. 2015; 7:16890. [PubMed: 26412614]
30. Arami H, Ferguson RM, Khandhar AP, Krishnan KM. Med Phys. 2013; 40:071904. [PubMed: 23822441]
31. Ferguson MR, Minard KR, Krishnan KM. J Magn Magn Mater. 2009; 321:1548. [PubMed: 19606261]
32. Park J, An K, Hwang Y, Park JG, Noh HJ, Kim JY, Park JH, Hwang NM, Hyeon T. Nat Mater. 2004; 3:891. [PubMed: 15568032]
33. Pu K, Chattopadhyay N, Rao J. J Control Release. 2016; 240:312. [PubMed: 26773769]
34. Cui L, Rao J. Nanomed Nanobiotechnol. 2017; 9:e1418.
35. Pu K, Shuhendler AJ, Jokerst JV, Mei J, Gambhir SS, Bao Z, Rao J. Nat Nanotechnol. 2014; 9:233. [PubMed: 24463363]
36. Geng J, Li K, Pu KY, Ding D, Liu B. Small. 2012; 8:2421. [PubMed: 22544732]
37. Zhang J, Zhen X, Upputuri PK, Pramanik M, Chen P, Pu K. Adv Mater. 2017; 29:1604764.
38. Howes P, Green M, Bowers A, Parker D, Varma G, Kallumadil M, Hughes M, Warley A, Brain A, Botnar R. J Am Chem Soc. 2010; 132:9833. [PubMed: 20572665]
39. Lu C-W, Hung Y, Hsiao J-K, Yao M, Chung T-H, Lin Y-S, Wu S-H, Hsu S-C, Liu H-M, Mou C-Y. Nano Lett. 2007; 7:149. [PubMed: 17212455]
40. Mailander V, Lorenz MR, Holzapfel V, Musyanovych A, Fuchs K, Wiesneth M, Walther P, Landfester K, Schrezenmeier H. Mol Imaging Biol. 2008; 10:138. [PubMed: 18297365]
41. Them K, Salamon J, Szwargulski P, Sequeira S, Kaul M, Lange C, Ittrich H, Knopp T. Phys Med Biol. 2016; 61:3279. [PubMed: 27032447]
42. Them K, Kaul MG, Jung C, Hofmann M, Mummert T, Werner F, Knopp T. IEEE T Med Imaging. 2016; 35:893.
43. Ferguson RM, Khandhar AP, Kemp SJ, Arami H, Saritas EU, Croft LR, Konkle J, Goodwill PW, Halkola A, Rahmer J. IEEE T Med Imaging. 2015; 34:1077.
44. Kaul MG, Mummert T, Jung C, Salamon J, Khandhar AP, Ferguson RM, Kemp SJ, Ittrich H, Krishnan KM, Adam G. Phys Med Biol. 2017; 62:3454. [PubMed: 28060771]
45. Graeser M, Knopp T, Szwargulski P, Friedrich T, von Gladiss A, Kaul M, Krishnan KM, Ittrich H, Adam G, Buzug TM. Sci Rep. 2017; 7:6872. [PubMed: 28761103]
46. Miao Q, Lyu Y, Ding D, Pu K. Adv Mater. 2016; 28:3662. [PubMed: 27000431]

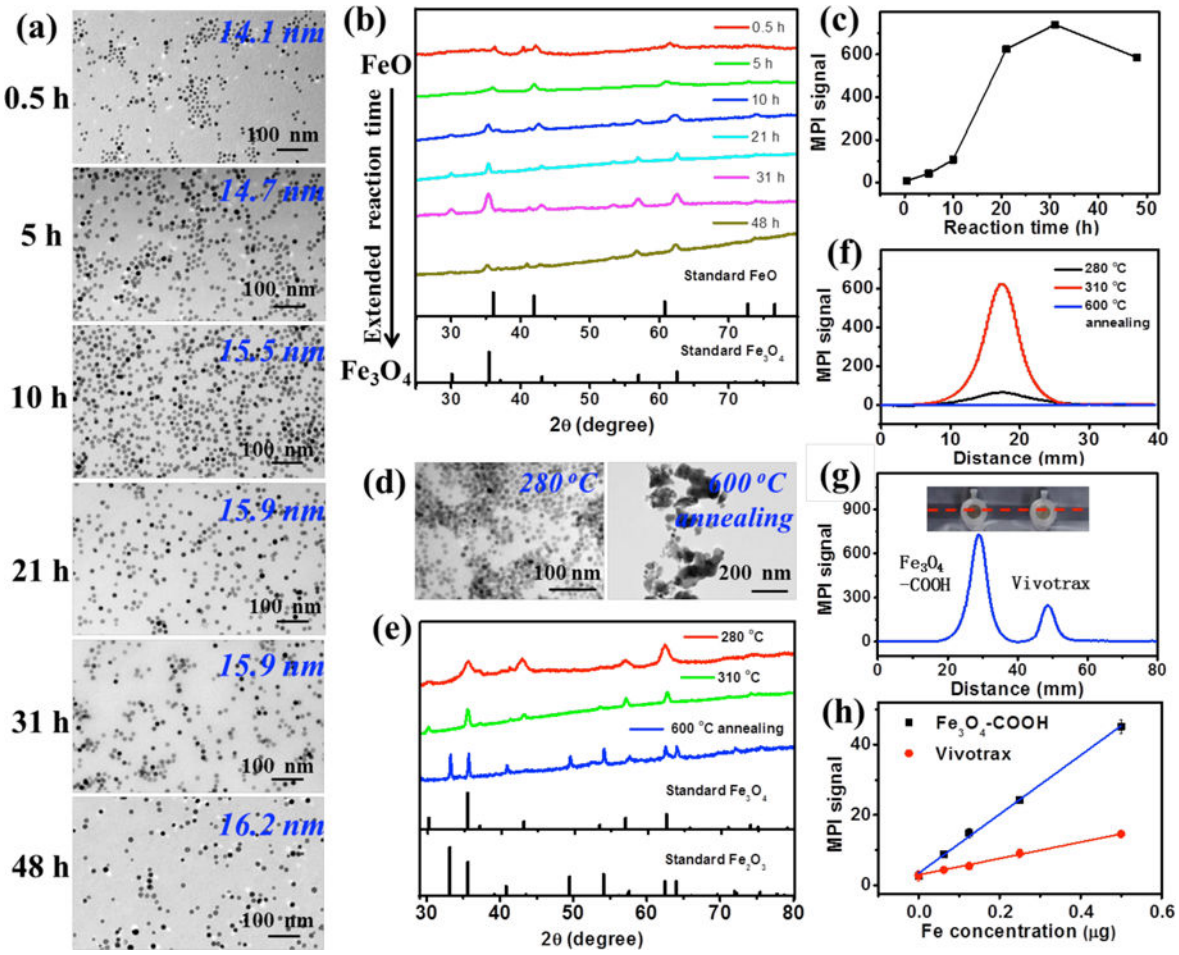

Figure 1.

(a–c) Characterization of iron oxide nanocrystals synthesized by thermal decomposition of an iron-oleate complex at 310 °C with various reaction times (e.g. 0.5, 5, 10, 21, 31, 48 h). (a) TEM images of iron oxide nanoparticles synthesized at 310 °C. (b) Powder XRD patterns of iron oxide nanoparticles synthesized at 310 °C. (c) MPI peak signals of PSMA-modified iron oxide nanoparticles synthesized at 310 °C with the same amount of Fe (8 μg) in 200 μL H_2O. (d–f) Characterization of iron oxide nanocrystals synthesized by thermal decomposition of an iron-oleate complex at 21 h with 280 °C and 310 °C, and iron oxide nanocrystals (prepared at 310 °C / 21 h) annealed at 600 °C for 2 h in air atmosphere. (d) TEM images of as-prepared iron oxide nanoparticles. (e) Powder XRD patterns of as-prepared iron oxide nanoparticles. (f) Linear scanning MPI spectra of as-prepared iron oxide nanoparticles with the same amount of Fe (8 μg) in 200 μL H_2O. (g) Photograph of PCR tube containing 200 μL of Fe_3O_4-COOH (prepared at 310 °C / 31 h) and Vivotrax with the same amount of Fe (8 μg), and corresponding linear scanning MPI spectra. (h) Plot of the MPI signals of Fe_3O_4-COOH (prepared at 310 °C / 31 h) and Vivotrax versus the amount of Fe in 200 μL H_2O.

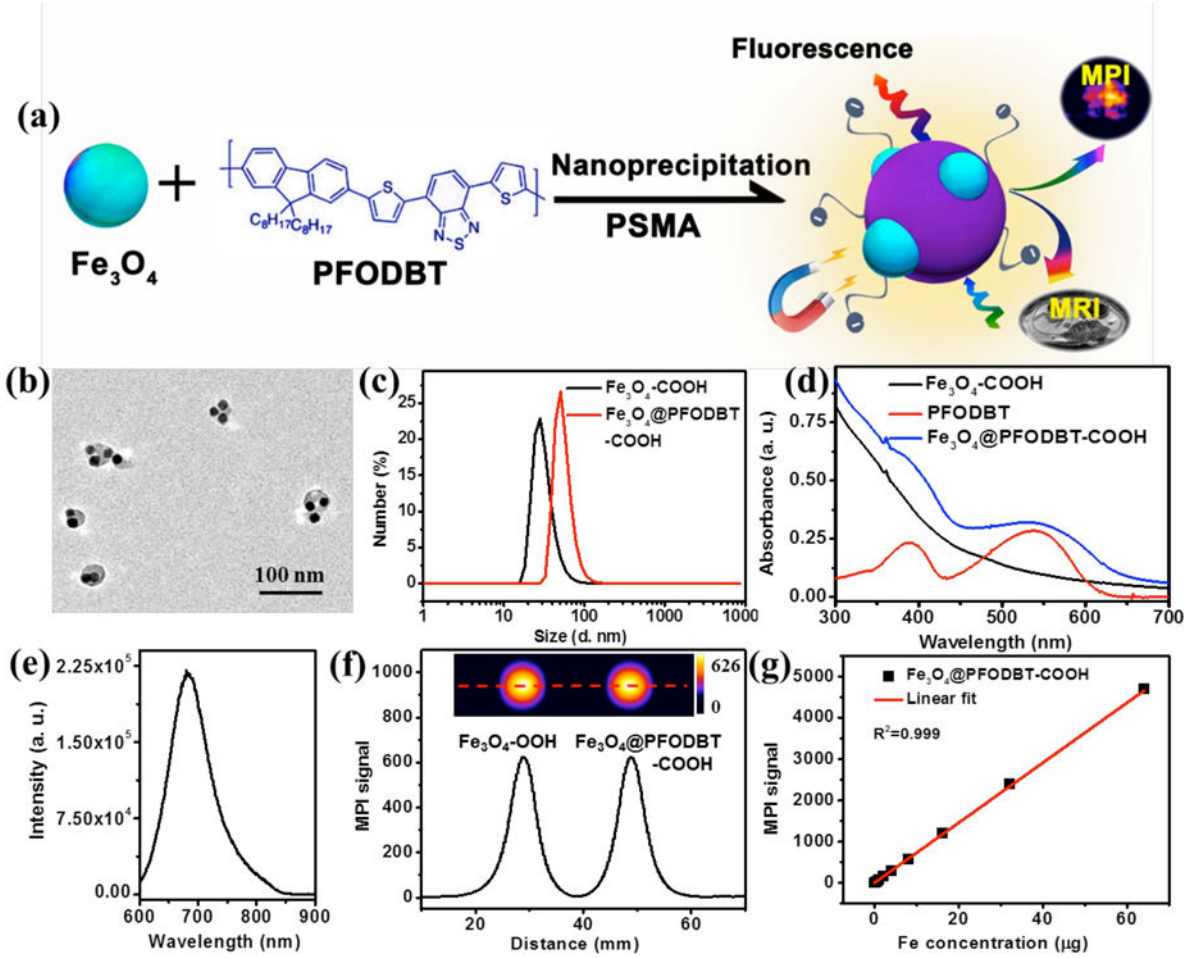

Figure 2.

(a) Schematic of the preparation of Fe_3O_4@PFODBT-COOH Janus nanoparticles through nanoprecipitation. (b) TEM image of Fe_3O_4@PFODBT-COOH Janus nanoparticles. (c) DLS size of Fe_3O_4-COOH and Fe_3O_4@PFODBT-COOH in PBS. (d) UV-vis absorption spectra of PFODBT in THF, and Fe_3O_4-COOH and Fe_3O_4@PFODBT-COOH in PBS. (e) Fluorescence spectrum of Fe_3O_4@PFODBT-COOH (excited at 540 nm). (f) Two-dimensional projection MPI scanning of Fe_3O_4-COOH and Fe_3O_4@PFODBT-COOH with the same amount of Fe (8 μg) in 200 μL H_2O, and their corresponding linear scanning MPI spectrum. (g) Plot of MPI signals of Fe_3O_4@PFODBT-COOH versus amounts of Fe in 200 μL H_2O.

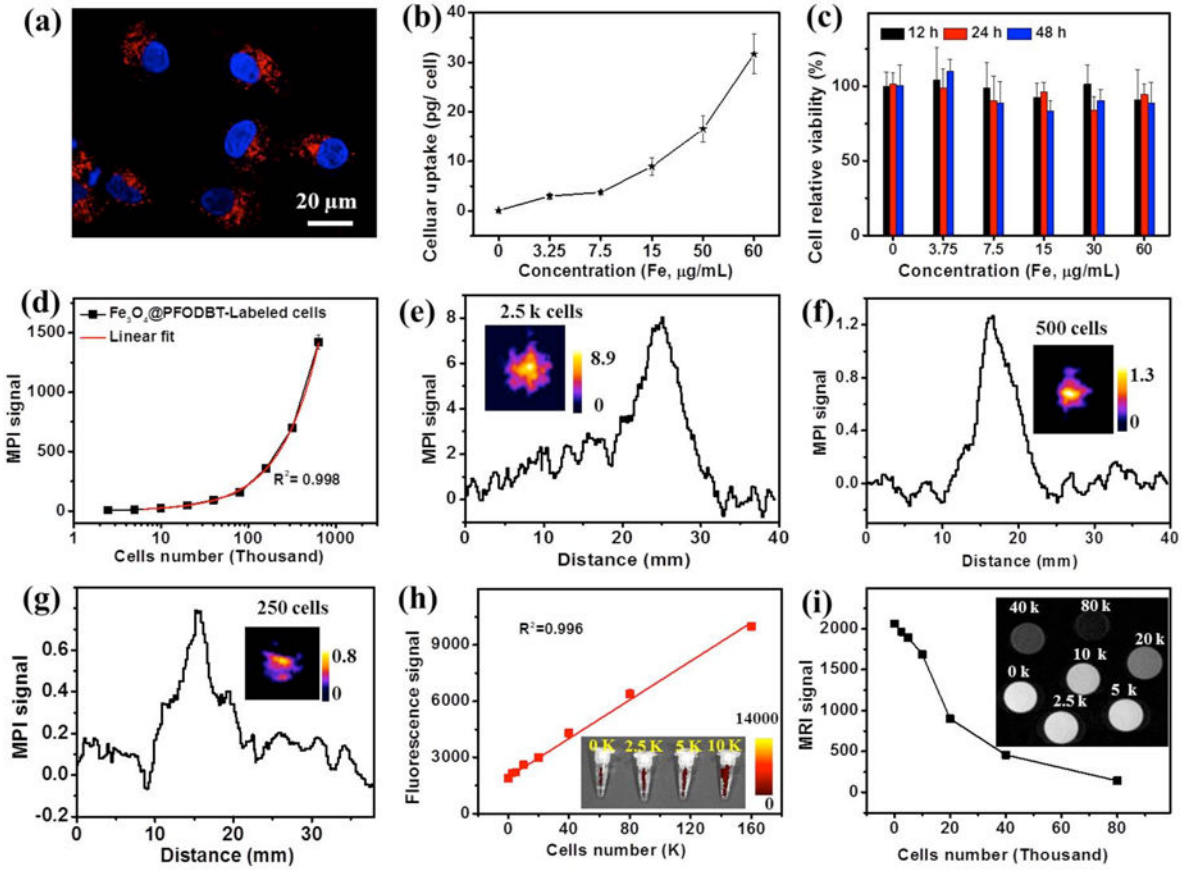

Figure 3.

(a) Internalization of Fe_3O_4@PFODBT-COOH by HeLa cells observed by confocal laser scanning microscopy. The cells were incubated with 60 μg Fe /mL of Fe_3O_4@PFODBT-COOH for 4 h, then fixed and stained with DAPI. Blue fluorescence shows nuclei stained with DAPI and red fluorescence shows the location of Fe_3O_4@PFODBT-COOH. (b) Plot of cellular uptake of particles with the incubation concentration, determined by ICP. (c) MTS assay of proliferation of Fe_3O_4@PFODBT-COOH labeled cells in fresh cell medium for indicated periods of time. (d) Plot of MPI signals versus the number of Fe_3O_4@PFODBT-COOH labeled cells (31 pg Fe /cell) from 2.5 K to 640 K in 200 μL PBS in PCR tubes. (e) Linear scanning MPI spectra of 2500 labeled cells (31 pg Fe/cell) in 200 μL PBS in a PCR tube (inset is projection MPI image of 2.5 K cells). (f & g) Linear scanning MPI spectra of (f) 500 and (g) 250 labeled cells (31 pg Fe /cell) in 20 μL PBS in a PCR tube; inset is projection MPI image of labeled cells. (h) Plot of fluorescent signals versus the number of labeled cells ranging from 0 to 160 K (insert is fluorescent image of tubes containing 0 to 10 K cells). (i) Plot of T_2-weight MRI signals of labeled cells versus number of labeled cells from 0 to 80 K (inset is MRI image from 0 to 80 K).

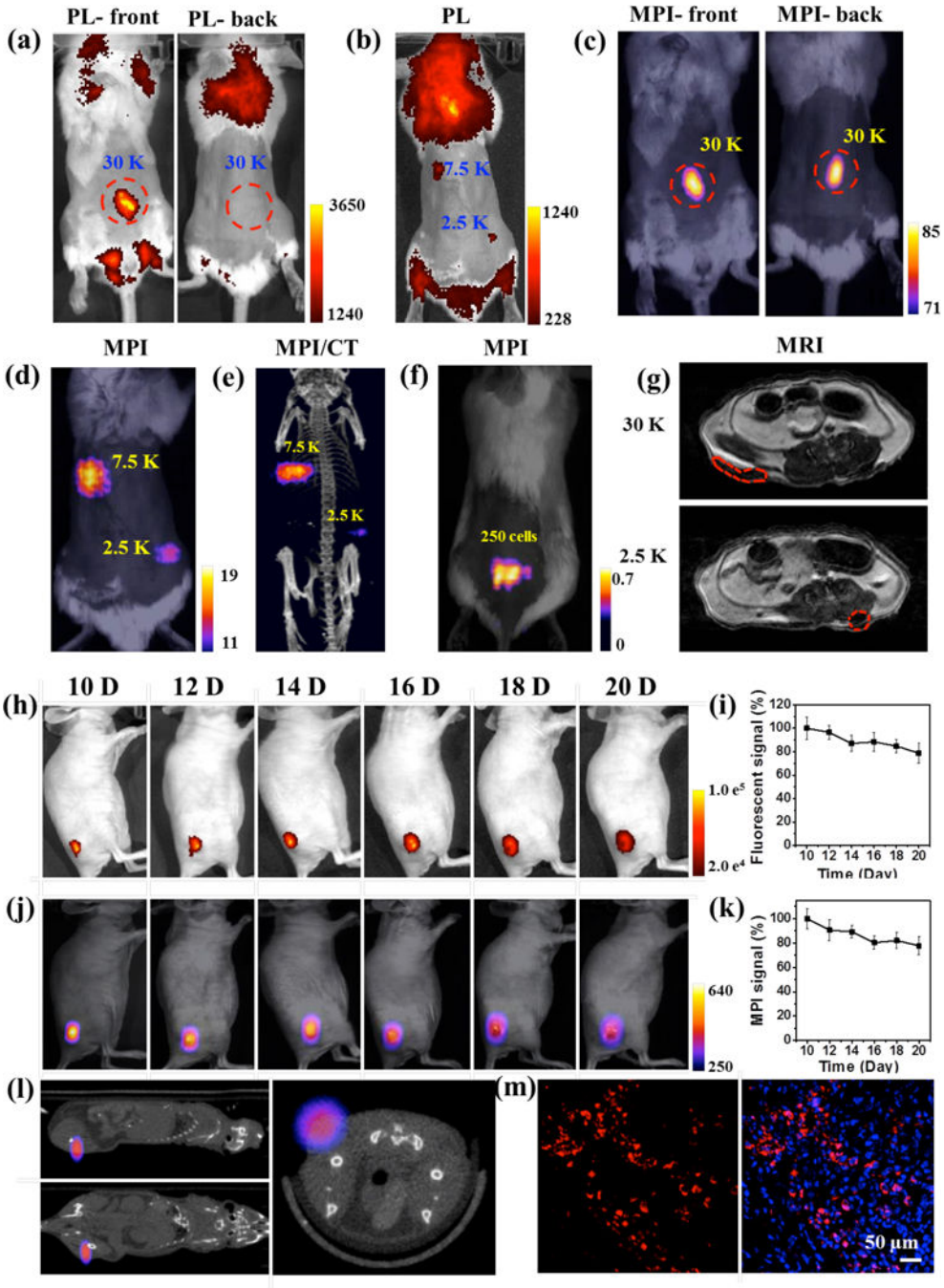

Figure 4.

(a & b) Fluorescence imaging of a mouse from front or back view after local subcutaneous injection of Fe_3O_4@PFODBT-COOH labeled cells (excitation: 540 nm; emission: 680 nm). (c & d) Two-dimensional projection MP imaging of mouse from front view or back view, after local subcutaneous injection of labeled cells. (e) Three-dimensional MPI and CT imaging of mouse after local subcutaneous injection of labeled cells. (f) Overlay of white light picture and 2-D projection MPI image of a mouse implanted 250 labeled cells after background subtraction. (g) MRI transverse images of mouse body after local subcutaneous

injection of cells labelled with Fe_3O_4@PFODBT-COOH. (h-m) *In vivo* tracking of HeLa cells xenograft tumor. The mice (n = 3) were subcutaneously implanted with Hela cells (3.5×10^5) pre-labeled with Fe_3O_4@PFODBT-COOH. (h) Longitudinal fluorescence images of a representative mouse at different time points (excitation: 540 nm; emission: 680 nm). (i) Quantification of fluorescence signals (%) of tumor areas as a function of post implantation time, relative to the value of day 10 post implantation. (j) Longitudinal two-dimensional projection MPI images of a representative mouse over 10 days. (k) Quantification of MPI signals (%) of tumor areas as a function of post implantation time, relative to the value of the 10th day post implantation. (l) Three-dimensional whole-body MPI and CT imaging of a representative mouse at the 20th day post implantation. (m) Confocal images of tumor slice on the 20th day after implantation. The tumors were frozen, sliced, fixed and stained with DAPI; blue fluorescence: nuclei stained with DAPI, red fluorescence: Fe_3O_4@PFODBT-COOH.